The seasonal anticyclonic circulation around the Qingdao cold water mass in the China marginal sea.

Lin Lin[1, a,*], Hans von Storch[1], Yang Ding[2]

[1]Institute of Coastal Systems, Helmholtz Zentrum Hereon, Geesthacht, 21502, Germany
[2]Frontier Science Center for Deep Ocean Multispheres and Earth System (FDOMES) and Physical Oceanography Laboratory, Ocean University of China, Qingdao, 266100, China
[a]Currently at Max Planck Institute for Meteorology, Hamburg, 20146, Germany

Correspondence to: Lin Lin (lin.lin@mpimet.mpg.de).

Abstract. The circulation structure surrounding the Qingdao cold water mass in 2019 was investigated via three-dimensional ensembles of numerical simulations. This study reveals that a cold pool appears in early spring and reaches its peak in late May, and this pool is accompanied by a local seasonal anticyclonic circulation. Momentum diagnostics are utilized to determine the relationship between the cold pool and this circulation. The momentum results reveal that vertical friction cannot be ignored because of the shallow topography and surface wind stress; as a result, the geostrophic balance is no longer applicable in the Qingdao cold water mass region. Consequently, the horizontal temperature and salinity gradients induced by the cold pool structure do not directly result in anticyclonic circulation. Additional numerical experiments are conducted in which tidal forcing or wind forcing is excluded to understand the formation mechanism of this anticyclonic circulation. The t test results reveal that the difference between the control run and the ensemble experiments without tidal forcing (or without wind forcing) is statistically significant. Thus, both tidal forcing and wind forcing have a significant influence on the anticyclonic structure, although their impacts differ. Without tidal forcing, an unrealistically strong current appears throughout the domain. Moreover, the direction of the eastern side of the anticyclonic circulation is reversed. On the other hand, the wind forcing contributes to the magnitude of the anticyclonic circulation, especially in the western portion of the anticyclonic circulation. Additionally, subcirculation occurs vertically around the Qingdao cold water mass and is influenced by both wind and tidal forcings. The use of ensembles constitutes an innovation in the field of marginal ocean simulations.

1. Introduction

The Qingdao cold water mass was first identified in 1959 and occurs in deep waters below 25 m in the southeastern offshore region of Qingdao during the spring season (the position of Qingdao and the position mentioned in this paper are shown in Fig. 1) (Ho et al., 1959). This cold water mass is an isolated cold pool characterized by low temperature (6.5–10.0°C), moderate salinity (31.5–32.5), and seasonal variation (Zheng and Zhang, 1983). This cold water mass has a significant influence on aquaculture in China since it is situated near the Chinese coastline (Zhang, 1986; Zhang and Geng, 1989; Zheng and Zhang, 1983); the temperature, salinity, and circulation distribution of the Qingdao cold water mass play important roles in the ecosystem, such as in primary production (Wei et al., 2019). Numerous researchers have conducted surveys on the origin and characteristics of the Qingdao cold water mass and reported that it forms in late April, reaches its peak in May, and gradually moves eastward, with both the temperature and salinity increasing. After June, this cold water mass gradually disappears, as it merges with the bottom layer of the Yellow Sea (Diao, 2015; Yu et al., 2006; Zhang et al., 1994, 2004).

Although the Qingdao cold water mass lifetime is relatively short, it is considered an independent water mass because of its unique patterns of both formation and evolution. On the basis of observational data, Zhang et al. (2002) analyzed the source and temperature–salinity characteristics of the Qingdao cold water mass, indicating that it formed in the local environment by the Bohai Sea coastal current bypassing the Shandong Peninsula. This cold water mass is characterized by low temperature, moderate salinity, and high dissolved oxygen. Zhang et al. (2004) analyzed the intensity variations in the Qingdao cold water mass, and their results suggest that it disappears gradually in June and July. However, some studies have observed the presence of the Qingdao cold water mass in August (Xia and Xiong, 2013). Yu et al. (2005, 2006) analyzed the relationship between the Qingdao cold water mass and the Yellow Sea cold water mass and reported that in June, the Qingdao cold water mass was already on the edge of the Yellow Sea cold water mass; it was no longer a local independent water mass but rather a local cold center within the Yellow Sea cold water mass. Huang et al. (2019) used numerical simulations to reveal that the cold and moderate-salinity water in the offshore area between Qingdao and Shidao in the southwestern Yellow Sea was an early form of the Qingdao cold water mass. Additionally, the strong horizontal temperature gradient is the thermodynamic mechanism by which the Qingdao cold water mass forms (Zhang et al., 2016). On the basis of the previous research mentioned above, conclusions have been drawn regarding the seasonal variations and origins of the Qingdao cold water mass. Previous work has demonstrated that a mesoscale anticyclone exists near the Qingdao coast, and its position is close to the Qingdao cold water mass (Huang et al., 2019; Zhang et al., 1987).

There are other cold water masses in the Bohai and Yellow Seas, the marginal seas along China, such as the cold pool in the Bohai Sea (Liu et al., 2003; Wan et al., 2004; Zhou et al., 2017) and the Yellow Sea cold water mass (Ho et al., 1959; Hur et al., 2000; Wei et al., 2010; Yuan et al., 2013). The special circulation structures around the Bohai cold water mass and Yellow Sea cold water mass have been well described in previous research (Wang et al., 2014; Xia et al., 2006; Zhou et al., 2017; Zhu and Wu, 2018), but the anticyclone current field analysis near the Qingdao cold water mass still needs to be investigated. In this work, we investigate the following questions: (1) Is the Qingdao cold water mass causing the local seasonal anticyclonic structure? Does such a seasonal anticyclonic circulation fit the geostrophic balance? (2) What factors influence the morphology, magnitude, and position of seasonal anticyclonic circulation horizontally and vertically?

The paper is organized as follows. The model configuration and model design are described in section 2. In this section, the concept and logic of ensemble simulations and the need to consider the internal variability of the marginal sea are described. Section 3 shows the results of the ensemble mean of the control simulations with respect to the simulated temperature, salinity, circulation structure, and momentum balance in the Qingdao cold water mass. In section 4, potential factors affecting the horizontal circulation pattern and the upwelling structures of the Qingdao cold water mass are discussed. Finally, conclusions are given in section 5.

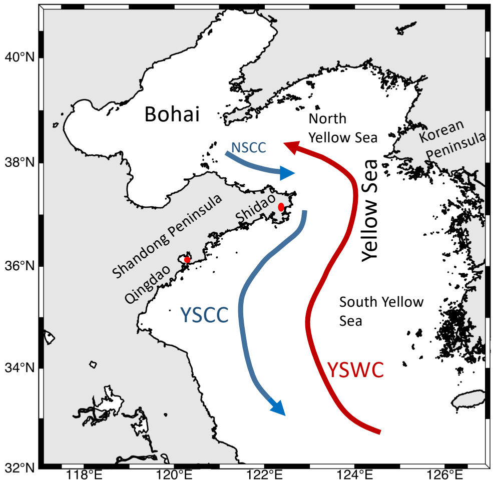

Figure 1. Maps of the Bohai Sea, Yellow Sea (North and South Yellow Seas), Shandong Peninsula, Korean Peninsula, Shidao, Qingdao, North Shandong Coastal Current (NSCC), and Yellow Sea Coastal Current (YSCC).

2. Methods and model

2.1 Model configuration

In this work, we use the three-dimensional unstructured grid finite volume coastal ocean model (FVCOM) (Chen et al., 2003, 2006). The horizontal grid resolution is approximately 4 km in the Bohai Sea and 8 km in the Yellow Sea. Vertically, the model consists of 30 sigma layers. The vertical and horizontal diffusion coefficients are calculated via the Mellor and Yamada level 2.5 (MY-2.5) turbulent closure model (Mellor and Yamada, 1982) and the Smagorinsky eddy parameterization method, respectively. The model domain includes the Bohai and Yellow Seas, ranging from 31.885°N to 40.942°N and from 117.572°E to 126.915°E, respectively (Fig. 1 in Lin et al. (2023)). The open boundary across the Yellow Sea extends from Qidong in China eastward to the southern tip of the Korean Peninsula, and radiation boundary conditions are used. For the control run, the six-hourly surface forcing data utilized in this study are from the National Centers for Environmental Prediction (NCEP) Climate Forecast System Version 2 (CFSv2) data, featuring a global resolution of 0.2°×0.2°(Saha et al., 2014). This dataset encompasses parameters such as sea surface temperature, cloud cover, air pressure, wind, specific humidity, evaporation, precipitation, and heat flux. The initial data of the model are introduced in the following ensemble experimental design section. The tidal elevation forcing is composed of 8 major tidal components ($\mathrm{M_2}$, $\mathrm{S_2}$, $\mathrm{N_2}$ $\mathrm{K_2}$, $\mathrm{K_1}$, $\mathrm{O_1}$, $\mathrm{P_1}$, and $\mathrm{Q_1}$) derived from the TPXO8 database (Egbert and Erofeeva, 2002). The model-simulated elevation, temperature, salinity, and circulation patterns were validated by Huang et al. (2019) and Lin et al. (2022, 2023). In this study, we focus directly on the analysis and discussion of the Qingdao cold water mass.

2.2 Ensemble experimental design

We first used an ensemble of control runs to analyze the temperature, salinity, and velocity around the Qingdao cold water mass. Additionally, we conducted two further ensembles of model experiments. One experiment was performed with tidal forcing turned off to examine the effect of tides on the Qingdao cold water mass, and another experiment was performed with wind forcing turned off (zero wind stress) to test the effect of the wind. The model output interval is three hours. A more thorough description of the ensemble simulation configuration can be found in Lin et al. (2022).

Ensemble simulations are conducted for the control run, no-tide run, and no-wind run. Each ensemble simulation consists of four numerical simulation members. In each ensemble, the initial conditions of the four simulations are taken from 1st Nov. of the 7th year, 1st Jan. of the 8th year, 1st Mar. of the 8th year, and 1st Nov. of the 8th year of the separate 9-year climatological simulation. Note that we conducted an independent 9-year simulation to generate slightly different but generally consistent initial conditions for the ensemble simulation. The model starting time of the 9-year climatological simulation was 1st Nov. 2008, and the model ending time was 31st Dec. 2019. The climatological forcing for the climatological run is a smooth annual cycle without weather variations based on National Centers for Environmental Prediction (NCEP) Climate Forecast System Version 2 (CFSv2) data. For the control run, no-tide run and no-wind run, the results for 2019 were used for further analysis. The model ending dates of the control run, no-tide run and no-wind run are 31st December 2019. The model output interval is three hours.

The motivation for using ensemble simulations is based on the observation (Lin et al., 2022, 2023; Penduff et al., 2019) that deviations form within the ensemble members if the ensemble simulations are conducted with the same model configuration except for slight perturbations in the initial conditions. In other words, if we have only one numerical simulation, the model output will be a mix of "signal" (external forcing) and random effects. Some spatial features are not repeatable in other ensemble members, even though the model configurations are the same. Averaging across ensemble simulations efficiently reduces the random impacts of randomness. Therefore, in Sections 3 and 4, we consider the ensemble means for further analysis. An ensemble simulation with slightly different initial conditions is one way to analyze ocean internal variability. For the ensemble simulation configuration in this study, we follow the tradition of generating an ensemble simulation with slightly different initial conditions (Penduff et al., 2019).

Because deviations exist between ensemble members because of randomness, we need to test whether the differences between the ensemble means of the control run and the no-tide run (/no-wind run) may be caused by external forcings (tidal or wind forcings) or could be caused only by randomness. A proper way to do so is statistical hypothesis testing with the null hypothesis: "external forcing has no effect". If this null hypothesis is rejected with a sufficiently small risk, then a valid conclusion is that an external factor has an effect and plays an active role. Here, a t test is performed for the ensemble monthly mean for May. The results (Figs. 2 and 3) show the sensitivity of the formation of the spring cold water mass to the presence of tidal forcing and wind forcing. Those grid points, at which a t test indicates that the effect of external forcing is significant, are marked with a cross. Figs. 2 and 3 demonstrate that the difference between the control run and the no-tide ensemble (or the /no-wind ensemble) is significant, especially where the intraensemble deviations are large.

When such local tests are conducted, one has to expect that even if the null hypothesis is valid, at approximately 5% of grid points, the null hypothesis is rejected (multiplicity of tests, cf. von Storch, and Zwiers, 1999). Since the rejection rate is itself a random variable, the false rejection rate can be much larger, but more than 20% is very unlikely. Here, the rate is considerably greater in both cases.

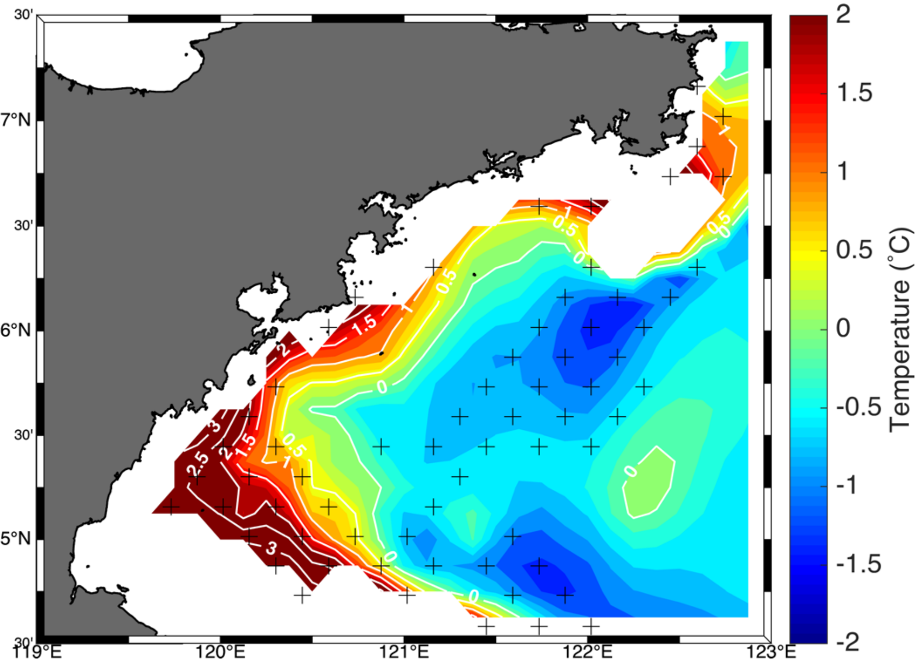

Figure 2. The difference in temperature between the ensemble means of the control runs and those of the runs without tidal forcing. The crosses represent the areas where the difference between the control run and the run without tidal forcing was significant at the 5% level.

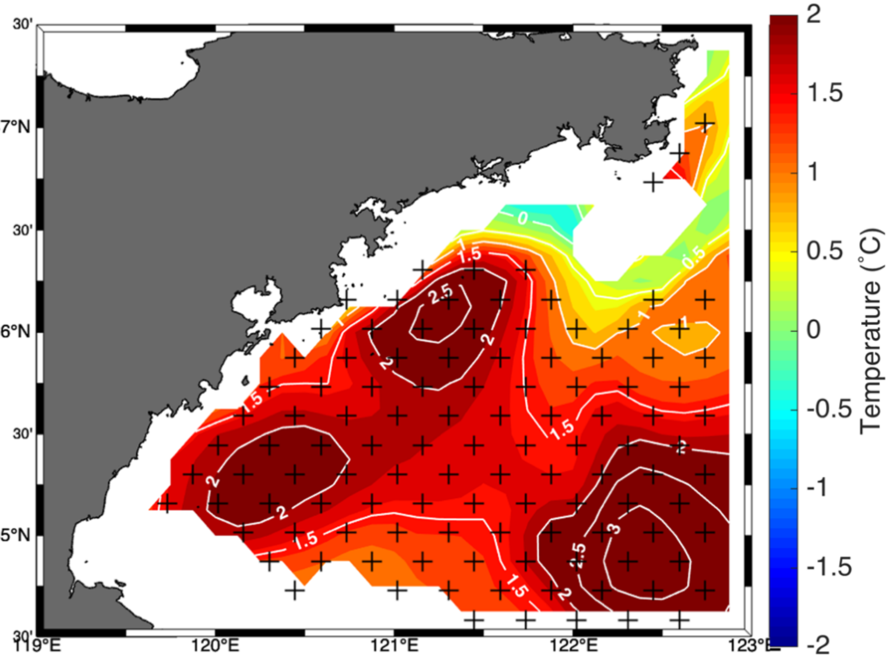

Figure 3. The difference in temperature between the ensemble means of the control runs and those of the runs without wind forcings. The crosses represent the areas where the difference between the control run and the run without tidal forcing was significant at the 5% level.

3. Results

3.1 Temperature and Salinity of the Qingdao Cold Water Mass

The temperature distribution at a depth of 25 m around the Qingdao cold water mass is shown in Fig. 4a-c. In March, the cold water carried by the Bohai coastal current approaches the area around the Shandong Peninsula, gradually evolving to become the Qingdao cold water mass, but the isotherms did not close, and the Qingdao cold water mass structure did not form at this time (Fig. A1). In April, a low-temperature tongue enveloped by an 8°C isotherm occurs north of 35°45′N and east of 121°45′E, accompanied by a horizontal temperature gradient. During this period, the high-temperature water transported by the northwest path of the Yellow Sea warm current remains in the western region of the South Yellow Sea, forming an apparent ocean front with the Qingdao cold water mass (Fig. 4a). In May, the location of the cold water mass center does not change at a depth of 25 m (Fig. 4b). Combined with the salinity results shown in Fig. 4d-f, it is clear that the temperature and salinity are relatively low around the Shandong Peninsula. Low-salinity water intrudes toward the south, and the intrusion direction is northeast–southwest, which is consistent with previous research results (Diao, 2015). The low-temperature and moderate-salinity water tongue along the northeast of the Shandong Peninsula merges with the ambient warm water left by the Yellow Sea cold water mass beginning in winter. In June (Fig. 4c), the temperature increases as the solar radiation increases, accelerating the merging of warm and cold water and causing the Qingdao cold water mass to disappear. Fig. 5 presents the vertical temperature distribution of the Qingdao cold water mass along the 35.625°N profile in May, revealing that the center of the cold water mass is 122.4°E, and there is an evident thermocline, which prohibits heat transport from the surface to the water below. The thermodynamic driving force for the formation of the Qingdao cold water mass is this strong thermocline. In summary, the Qingdao cold water mass starts to merge in April, continues to develop in May, is accompanied by a strong horizontal temperature gradient, and disappears in June. The cold water mass center is at 122.75°E 36.15°N, and the shape of the cold water mass has a northeast–southwest orientation.

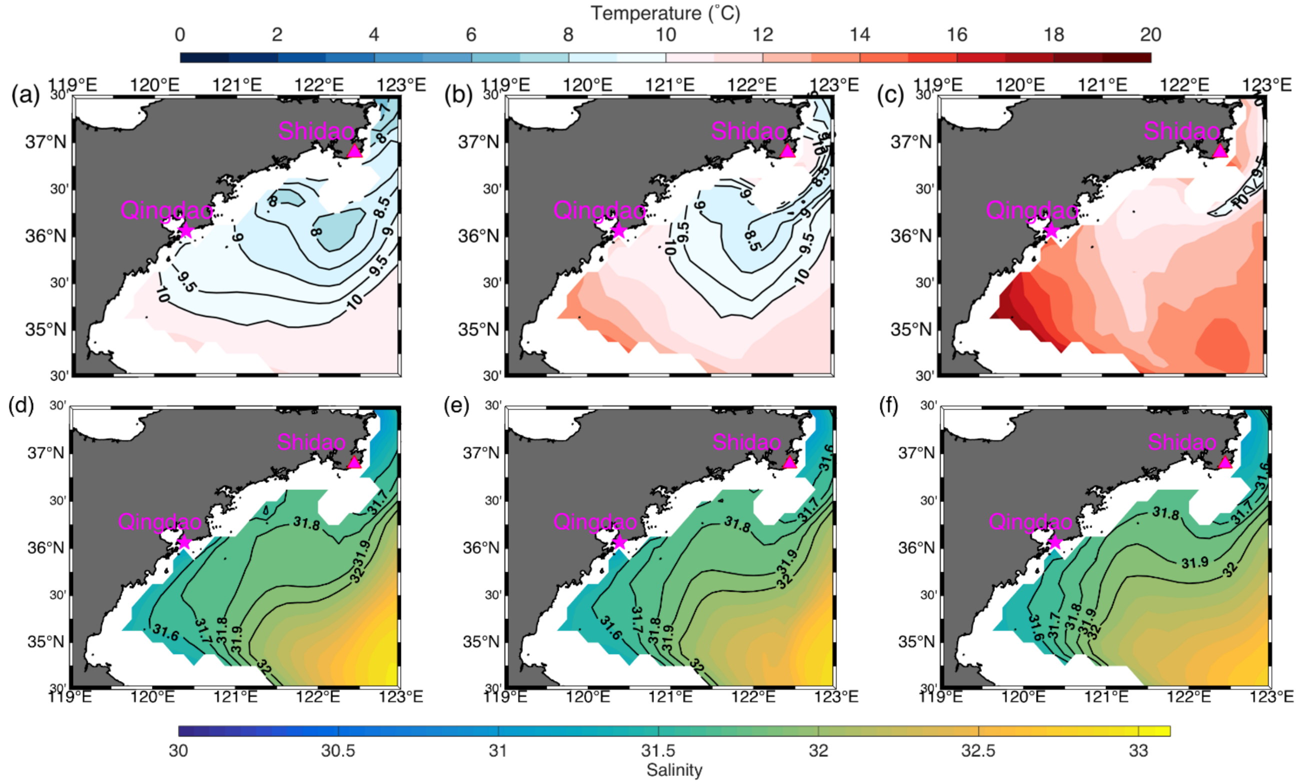

Figure 4. The monthly mean temperature and salinity evolution of the Qingdao cold water mass from April to June at a depth of 25 m according to the ensemble mean of the control runs. Figs. 4a, b, and c show the temperature distributions of the peaks of the Qingdao cold water mass (in April), the gradual disappearance (in May), and the complete disappearance (in June), respectively. Figs. 4d-f are the same as Figs. 4a-c but for salinity. To clearly present the temperature distribution, the isotherms between 8℃ and 10℃ are marked with 0.5℃ intervals.

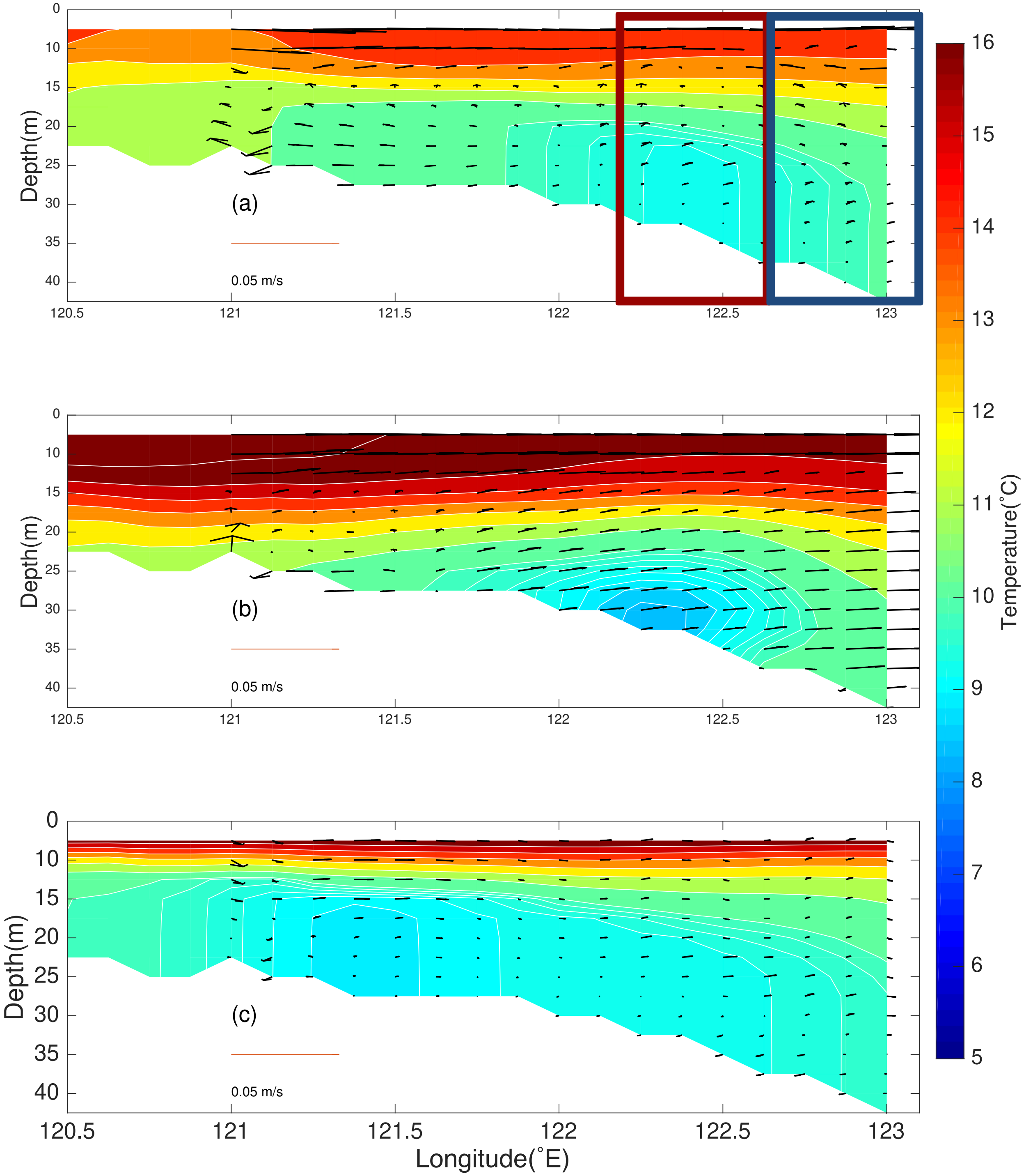

Figure 5. The temperature and zonal–vertical current along the 35.625°N profile in May in the ensemble means. For better visualization, the vertical velocity is multiplied by 1000 (unit: m/s). (a) Control run, (b) no-tide experiment, and (c) no-wind

experiment. The red and blue boxes represent the frontal zones (121.5-122°E and 122.625-123°E) on the western and eastern sides of the Qingdao cold water mass.

3.2 Circulation pattern

A seasonal anticyclonic structure exists near the Qingdao cold water mass. Fig. 6 shows the circulation at a depth of 25 m from April to June. In April, the seasonal anticyclonic structure is not closed. In May, a southeasterly monsoon prevails near the Shandong Peninsula, and a northward current can be seen along the Shandong Peninsula coastline, meeting the southward current between 122°E and 123°E. In May, the seasonal anticyclonic structure nearly closes, and the northeastward flow on the west side of the anticyclonic structure is stronger than the southwestward current on the east side. The center position of the seasonal anticyclonic circulation is 122.4°E, 35.5°N, and the velocity at the center of the anticyclonic circulation is very slow. In June, the seasonal anticyclonic circulation disappears when the southward current is strengthened (not shown). The above simulation results are consistent with those of previous works (Xu and Zhao, 1999; Zhang et al., 1987). As the water depth is shallow in the western portion of the anticyclonic circulation and the dominant southeasterly monsoon, the current velocities in the western part of the anticyclonic circulation are stronger than those in the eastern part.

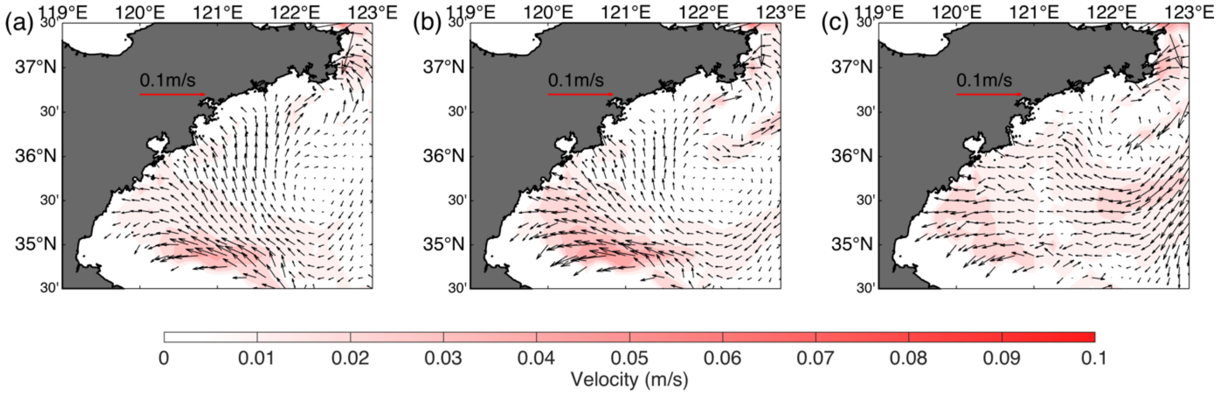

Figure 6. The horizontal circulation distributions around the Qingdao cold water mass (25 m layer) in April (a), May (b), and June (c).

The three-dimensional circulation pattern overlapping with the temperature is shown in Fig. 7. There is a cold water mass center in the 25 m layer, and the anticyclonic structure can still be observed at depths of 30 and 35 m. However, at depths greater than 35 m, the anticyclonic structure no longer exists. The patterns of the circulation structures in different layers are different, reflecting the baroclinic features of the current fields. At depths of 25, 30, and 35 m, the velocity increases as the horizontal temperature gradient around the edge of the cold pool increases. The unique seasonal anticyclonic circulation structure hinders horizontal heat transfer, which could serve as the dynamic mechanism for the formation of the Qingdao cold water mass (Huang et al., 2019).

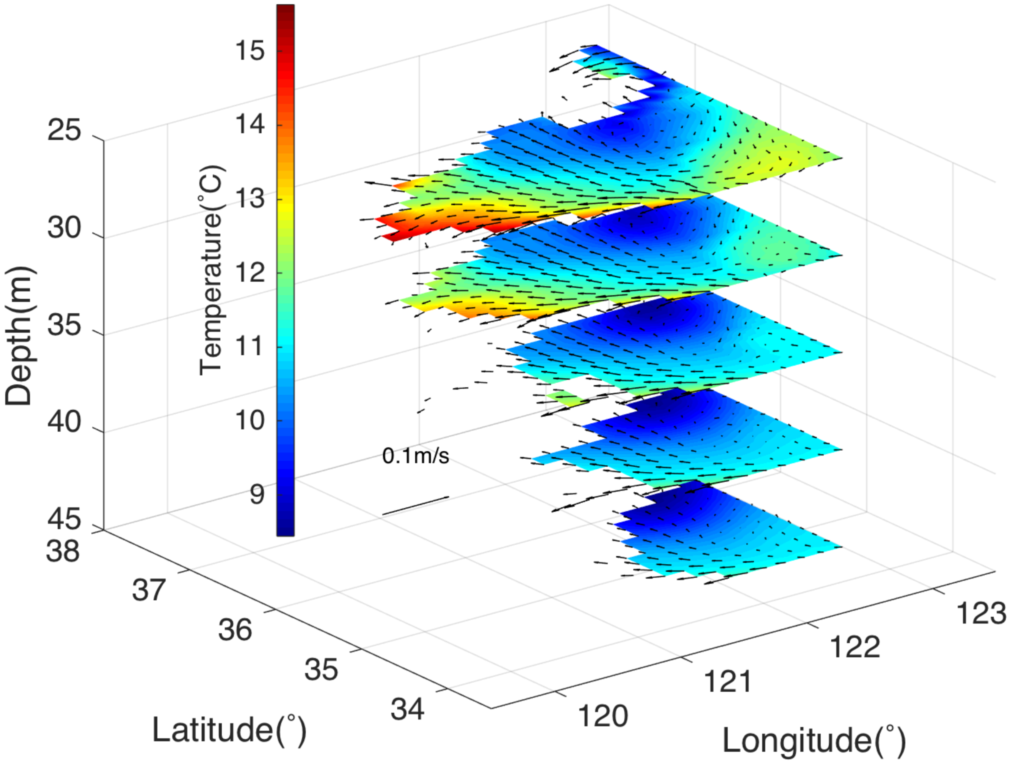

Figure 7. Three-dimensional structure of the Qingdao cold water mass in May at depths of 25, 30, 35, 40, and 45 m.

3.3 Momentum balance

$$\frac{\partial u}{\partial t}+u\frac{\partial u}{\partial x}+v\frac{\partial u}{\partial y}+w\frac{\partial u}{\partial z}-fv=-\frac{1}{\rho_o}\frac{\partial(p_H+p_a)}{\partial x}+\frac{\partial}{\partial z}\left(K_m\frac{\partial u}{\partial z}\right)+F_u \qquad (1)$$

$$\frac{\partial v}{\partial t}+u\frac{\partial v}{\partial x}+v\frac{\partial v}{\partial y}+w\frac{\partial v}{\partial z}+fu=-\frac{1}{\rho_o}\frac{\partial(p_H+p_a)}{\partial y}+\frac{\partial}{\partial z}\left(K_m\frac{\partial v}{\partial z}\right)+F_v \qquad (2)$$

To show the general pattern of the fundamental forces around the Qingdao cold water mass anticyclonic circulation region, we conduct a momentum balance diagnostic (see equations (1) - (2)). Taking the zonal direction as an example (equation (1)), the total pressure gradient term is $-\frac{1}{\rho_o}\frac{\partial(p_H+p_a)}{\partial x}$, which is composed of the barotropic pressure gradient force $g\frac{\partial\zeta}{\partial x}$ induced by sea level and the baroclinic pressure gradient force $\frac{1}{\rho}\frac{\partial}{\partial x}\int_z^\zeta \rho g dz$ induced by density; the Coriolis force $-fv$; the vertical friction term $\frac{\partial}{\partial z}\left(K_m\frac{\partial u}{\partial z}\right)$; the local velocity time variation term $\frac{\partial u}{\partial t}$; the horizontal advection term $u\frac{\partial u}{\partial x}+v\frac{\partial u}{\partial y}$; the vertical advection term $w\frac{\partial u}{\partial z}$; and the horizontal friction term F_u.

In both the 25 m and 40 m (Fig. 8) layers, the terms for the barotropic pressure gradient, baroclinic pressure gradient, Coriolis force, and vertical friction are dominant, and the other terms are far smaller (not shown). The barotropic gradient force is greater than the baroclinic gradient force and is balanced by the joint effects of the opposing baroclinic pressure gradient force, Coriolis force, and vertical friction force. Vertical friction is induced by wind stress from the surface layer (Fig. A2) and bottom friction from the bottom layer. In May, the southwesterly wind stress (Fig. A2) contributes to the northward current. Since the depth around the Qingdao cold water mass is relatively shallow, the friction caused by the tidal current and topography extends from the bottom layer to the middle layer, connecting with the wind stress from the surface layer, especially on the western side. Because there is vertical friction, a geostrophic balance no longer exists, especially in areas close to the coast. We address this issue in section 3.5.

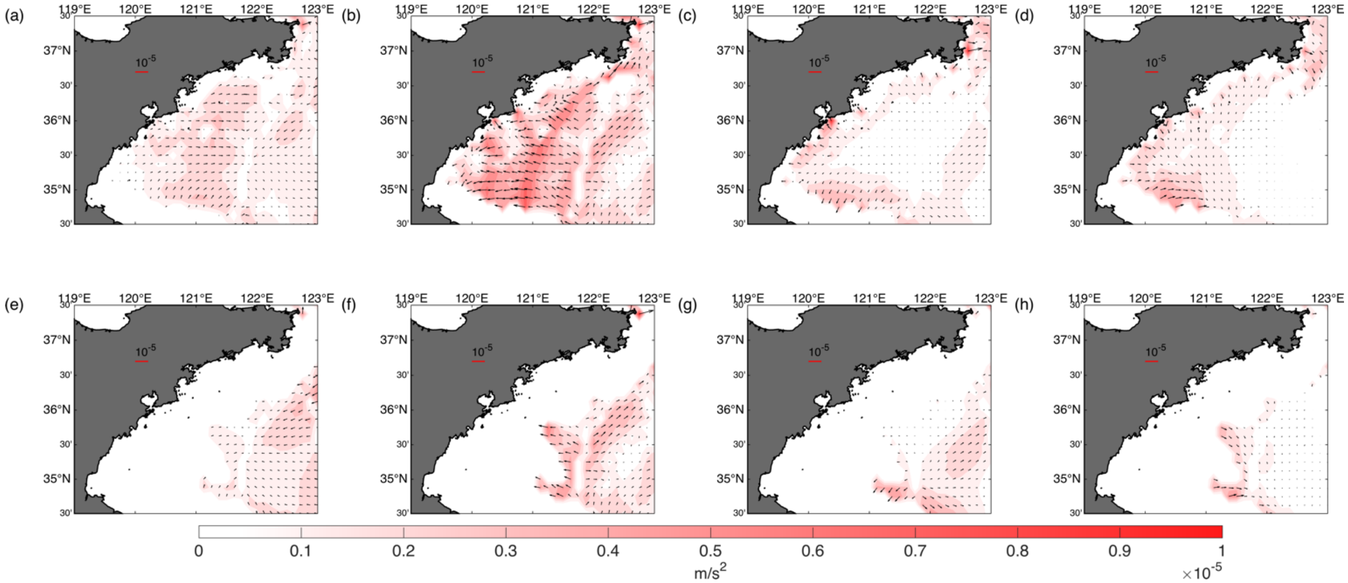

Figure 8. Horizontal distributions of momentum terms (monthly mean for May) at depths of 25 m (a-d) and 40 m (e-h): (a, e) Coriolis force, (b, f) barotropic pressure gradient force, (c, g) baroclinic pressure gradient force, and (d, h) vertical friction force. The color represents the magnitude of the momentum term.

3.4 Relation between the seasonal anticyclone circulation pattern and the Qingdao cold water mass

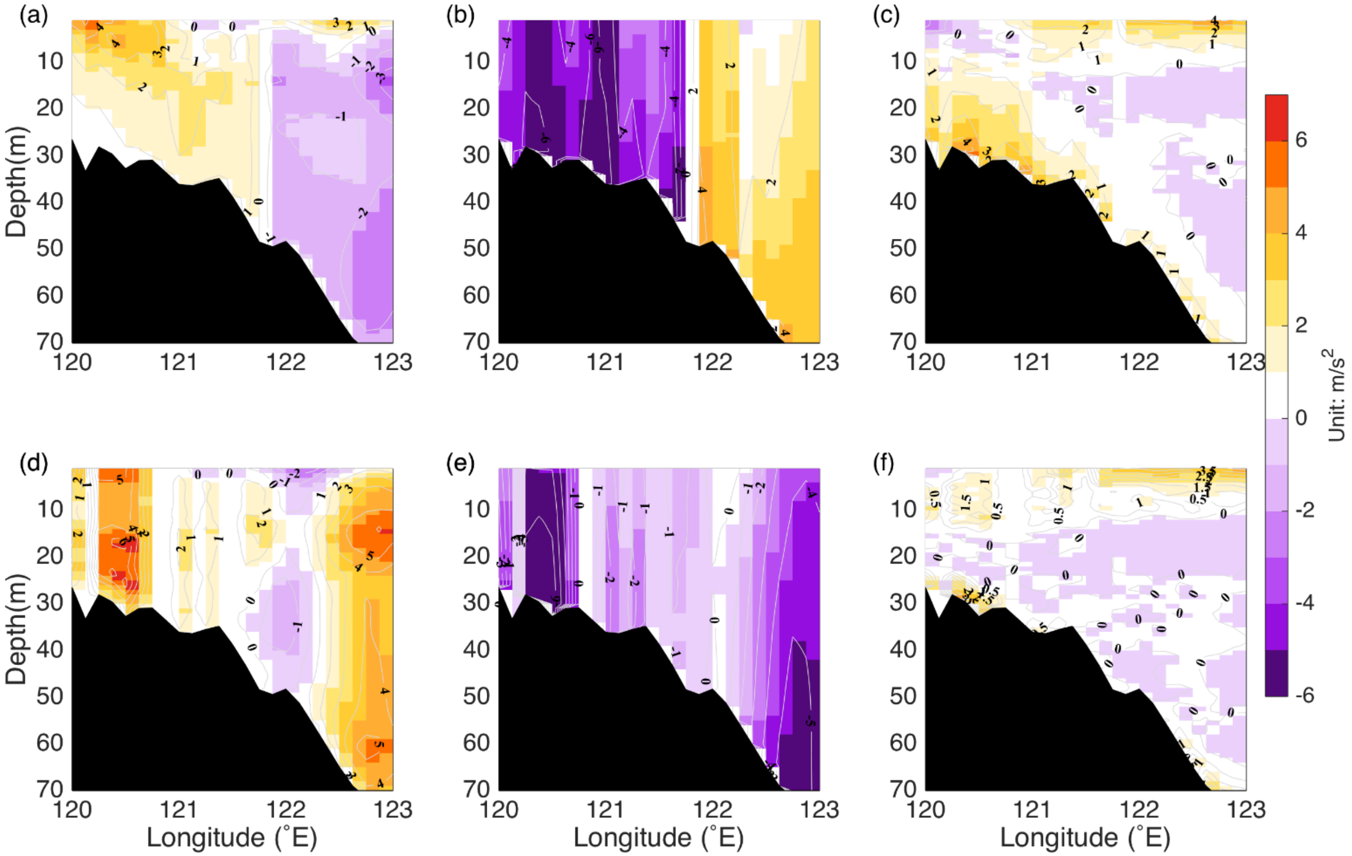

Figure 9. Vertical distribution of zonal momentum terms along the 35.5°N profile of the control run (a, b, c) and the no-tide experiment (d, e, f). (a, d) Coriolis force, (b, e) total pressure gradient force, (c, f) vertical friction force. The magnitude of the momentum terms has a time of 10^6 for visualization. A positive value represents the northward direction.

To further analyze the seasonal anticyclonic circulation around the Qingdao cold water mass, we show the vertical distributions of the Coriolis force, the total pressure gradient force, and the vertical friction force along the 35.5°N profile (Fig. 9). In the surface layer (0–10 m), west of 123°E, the total pressure gradient force is balanced by the combined effect of the Coriolis force and surface wind stress. In the middle layer (10–30 m), the Coriolis force is positive west of 122°E when the total pressure gradient is negative, whereas the region east of 122°E shows the opposite behavior. However, west of 122°E, the Coriolis force is not identical to the total pressure gradient force, indicating that the vertical friction force cannot be ignored, which is consistent with the conclusion drawn from the horizontal momentum balance distribution. The Ekman ratio is the ratio of the friction and Coriolis terms and represents the relative significance of the friction force (Fig. 10). The Ekman ratio is usually high in coastal areas. Fig. 10 shows that the Ekman ratio is much greater along the bottom layer in the control run, which indicates that the friction term again plays a significant role around the Qingdao cold water mass. Most importantly, the geostrophic balance is not valid west of 122°E, where anticyclonic circulation exists.

Because the geostrophic balance is not satisfactory in the western portion of the anticyclonic circulation, the anticyclonic circulation structure is not a direct result of the density gradient fronts, which are induced by the temperature and salinity gradients. This explains why an anticyclonic circulation appears around a cold temperature center caused by the Qingdao cold water mass. If the geostrophic balance is satisfied, then in the Northern Hemisphere, there should be an anticlockwise cyclonic circulation structure around a cold temperature center. The vertical friction completely disrupts the geostrophic balance.

To some extent, the seasonal anticyclonic circulation is the dynamic reason for the Qingdao cold water mass; this type of anticyclonic structure prohibits heat transfer between the cold temperature center and the surrounding water column (Huang et al., 2019), but the seasonal anticyclonic circulation is not caused by the special temperature and salinity structure around the Qingdao cold water mass.

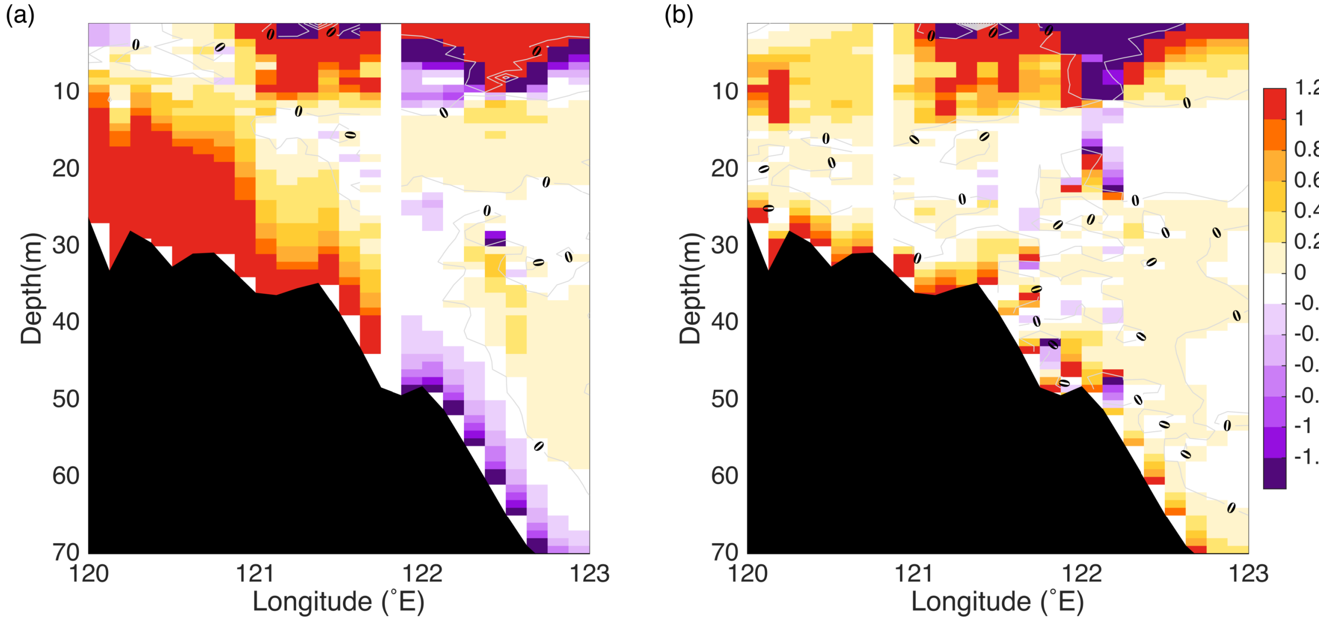

Figure 10. Vertical distributions of the Ekman ratio along the 35.5°N profile of the control run (a) and the no-tide experiment in the zonal direction.

4. Discussion

4.1 Tidal effects

In the Yellow Sea, tidal forcing plays a significant role in local circulation and modulates dissipation, vertical mixing, and tidal energy (Choi, 1980; Choi et al., 2003; Moon et al., 2009; Xia et al., 2006). A no-tide simulation is conducted to analyze the tidal forcing effect on the seasonal anticyclonic circulation around the Qingdao cold water mass. Fig. 11 shows the circulation pattern of the no-tide experiment in May at a depth of 25 m and the current deviations between the no-tide experiment and the control run; the results reveal that the circulation is different from that in the control run. Northward currents are present on the western side (to the west of 122°E) in the control run and in the no-tide experiment, but the magnitudes are significantly greater in the no-tide experiment. At the center of the anticyclonic circulation, changes in the current are not evident. When the tidal forcing is turned off, the eastern side of the anticyclonic circulation direction reverses, changing from a southward current (in the control run, see Fig. 6b) to a northward current. The clockwise circulation pattern disappears in the no-tide experiment. In the no-tide experiment, the current magnitude significantly increased throughout the region. This is because the friction is much lower than that in the control run, which is indicated by the momentum balance results (Fig. 12d).

The momentum diagnostic of the no-tide experiments shows that the magnitude of the velocity decreases compared with that of the control run. When tidal forcing is not considered, the vertical friction along the bottom layer becomes much smaller than that in the control run. Without tidal forcing east of 122°E, the total pressure gradient and Coriolis terms change direction, which is combined with a change in the circulation direction, indicating the significance of the tides around the anticyclonic circulation. In addition, the magnitude of the current in the entire region significantly increases, which is not realistic, indicating that the dissipation and friction caused by tidal forcing are important for modulating circulation in anticyclonic areas.

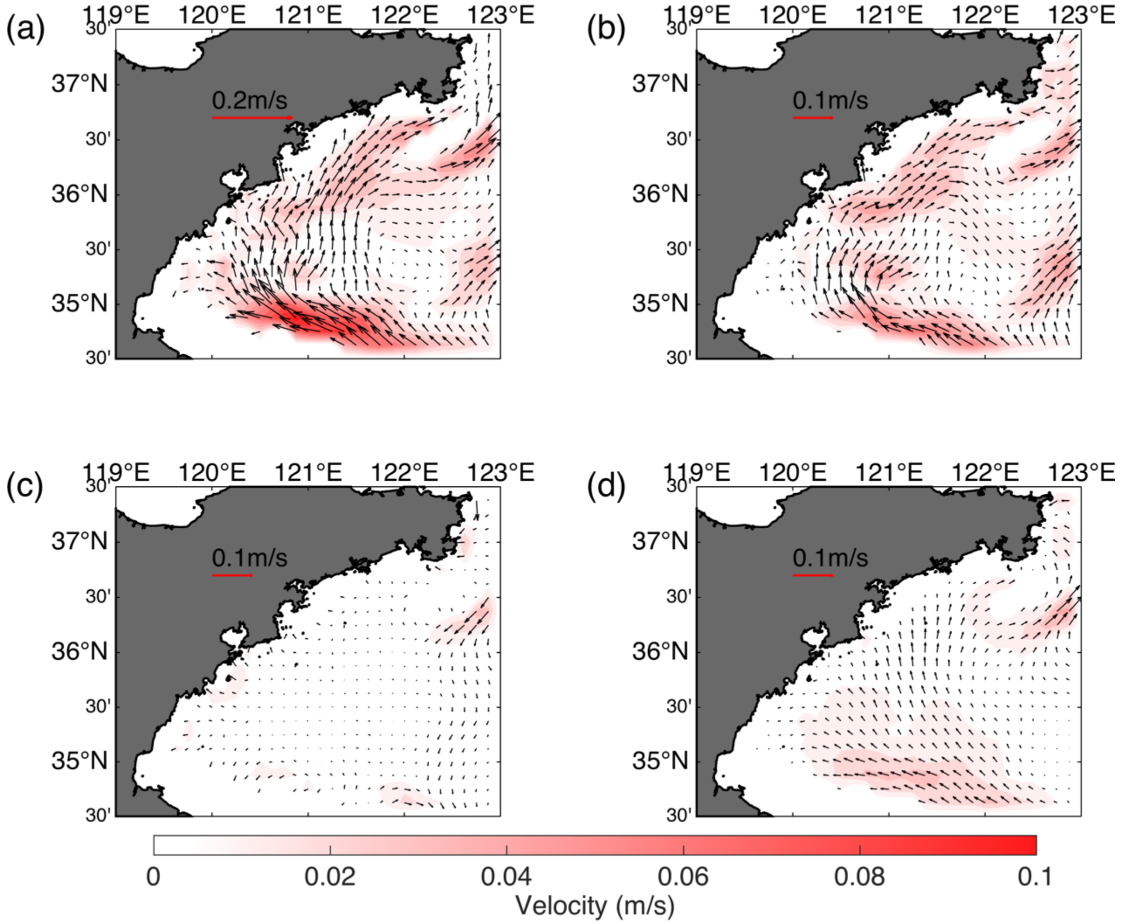

Figure 11. The impacts of tidal forcing and wind forcings on anticyclonic circulation in May at 25 m; (a) the circulation pattern of the no-tide experiment, (b) the difference between the no-tide experiment and the control run (no-tide experiment minus the control run), (c) the circulation pattern of the no-wind experiment, and (d) the difference between the control run and the no-wind experiment (control run minus the no-wind experiment).

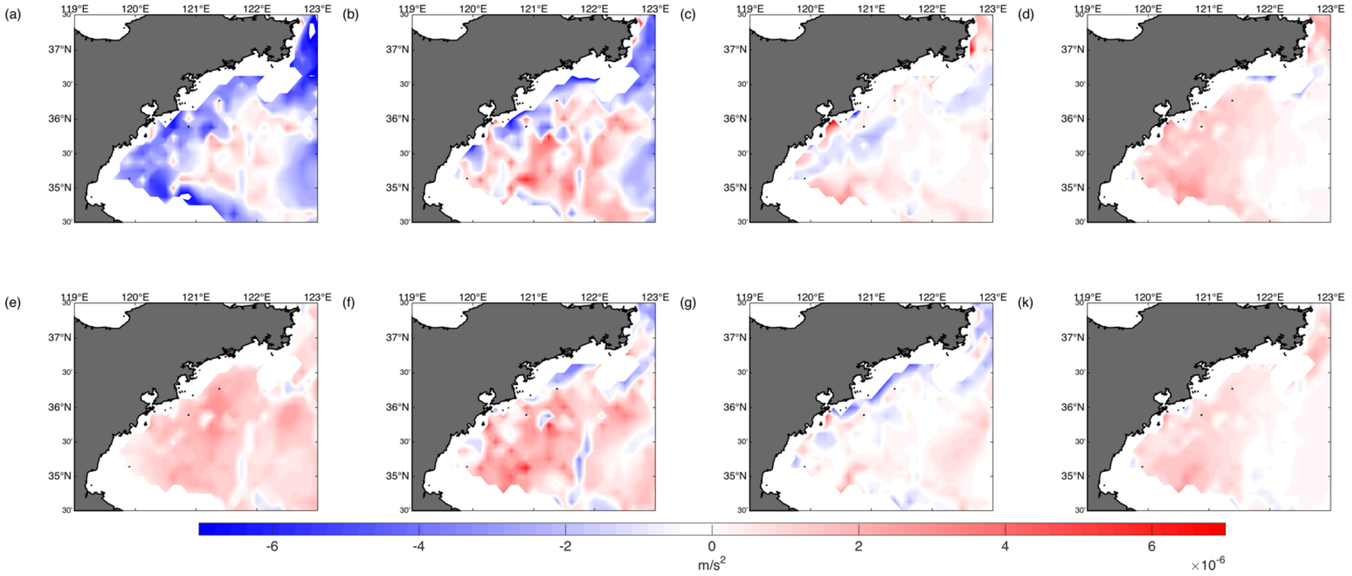

Figure 12. At 25 m, the momentum balance terms between the control run and the no-tide experiment (a-d) (control run minus no-tide experiment) and between the control run and no-wind experiment (e-k) (control run minus no-wind experiment) are shown. (a, e) Coriolis force, (b, f) barotropic pressure gradient force, (c, g) baroclinic pressure gradient force, and (d, k) vertical friction term. The results are the monthly means for May.

4.2 Wind effects

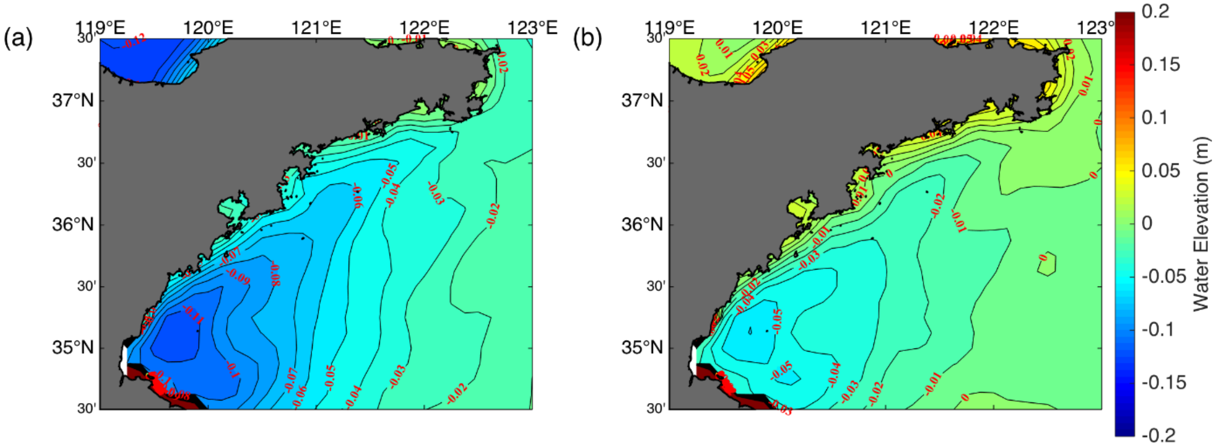

Figure 13. The surface elevation distributions of the control run (a) and the no-wind experiment (b). The monthly mean for May.

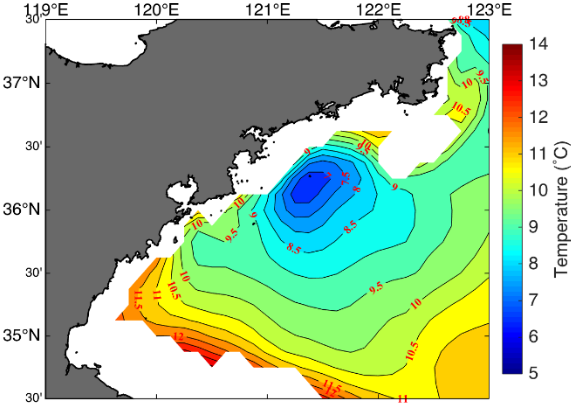

Figure 14. The horizontal temperature distribution at 25 m in the no-wind experiment (monthly mean for May).

Xu and Zhao (1999) demonstrated the effect of wind on the seasonal anticyclonic circulation around the Qingdao cold water mass via a 2D numerical model, but a more thorough discussion is needed. Therefore, we conducted a no-wind experiment to examine the effect of wind on the seasonal anticyclonic circulation structure. The results show that wind is a dominant driving force for clockwise circulation. The general magnitude of the current weakens, particularly on the western side of the clockwise circulation (northward current), confirming again that the southerly wind along the Shandong Peninsula is the cause. In contrast, the influence of wind on the eastern side of the circulation is minor, as shown in Figs. 11c and 11d. The direction and magnitude of the eastern side are similar to those of the control run.

To compare the momentum changes and further analyze the wind forcing effect in this area, we show the difference in the momentum changes between the control run and the no-wind experiment (control run minus the no-wind experiment, Fig. 12e-k). The Coriolis force decreases because of the weaker current when the wind forcing is turned off. The barotropic gradient force increases when wind forcing is considered, indicating that the variation caused by water elevation is greater with increasing wind forcing. The surface elevation data are shown in Fig. 13. With a southerly wind, the water surface is lower west of 121°E in the control run, indicating that the pressure gradient force distribution varies in the no-wind experiment. On the other hand, in the absence of mixing caused by surface winds, the temperature of the Qingdao cold water mass decreased by 2°C (Fig. 14), resulting in an increase in the baroclinic pressure gradient force around the location of the Qingdao cold water mass in the no-wind experiment. The vertical friction somewhat decreases because of the lack of wind stress in the no-wind experiment.

4.3 Upwelling

Vertically, upwelling occurs from the surface layer to the bottom layer near the Qingdao cold water mass, accompanied by relatively weak downwelling at the surface layer. Fig. 5a shows the vertical circulation structure in May at 35.625°N, which is around the horizontal center of the seasonal anticyclonic circulation. Upwellings occur near the frontal zones (121.5-122°E and 122.625-123°E) on the eastern and western sides of the Qingdao cold water mass, respectively. The seawater lifted by upwelling from the western and eastern sides of the cold pool converges toward the center, forming a downwelling in the surface layer at 122.5°E, but this downwelling is weak compared with the strength of upwelling.

We hypothesize that the upwelling in the western portion (121.5-122°E) is influenced mainly by wind forcing, which is Ekman upwelling. For the western portion (122.625-123°E), the wind forcing still plays a role, but for the eastern portion, tidal forcing contributes more to upwelling. The tidal mixing front generates a pressure gradient force, which strengthens the upwelling intensity on the east side. To test our hypothesis, we further analyzed the vertical circulation along the 35.625°N profile in May of the control run, the no-tide experiment, and the no-wind experiment (Fig. 5). To clearly visualize the vertical circulation, a separate vertical speed contour map overlapping with the temperature contours is plotted (Fig. 15). Fig. 5 shows that in the control, an eastward flow occurs west of 122.375°E (red rectangle), and a westward flow occurs east of 122.625°E (blue rectangle).

A comparison of Fig. 15a and 15c reveals that upwelling cycles occur in the red and blue rectangles in the control run, but in the no-wind experiment (Fig. 15c), the magnitude of upwelling cycling in the red rectangle decreases, as shown in Fig. 15c. In contrast, the impact of the wind forcing on upwelling in the eastern portion (122.5-123°E) is weaker than that in the western portion (Figs. 15c and 15f). Wind forcings have a significant impact on upwelling in the western portion of the Qingdao cold water mass (122-122.375°E).

In the no-tide experiment (Fig. 15b), the magnitude of upwelling is the same as that in the control run on the west side of the Qingdao cold water mass (to the west of 122.375°E), but on the east side of the Qingdao cold water mass, the magnitude of upwelling decreases. Therefore, we conclude that tidal forcing mainly affects upwelling on the east side of the Qingdao cold water mass. Additionally, the zonal velocity greatly increases when the tidal forcing is turned off, mainly because friction decreases in the no-tide experiment, as discussed in section 4.1.

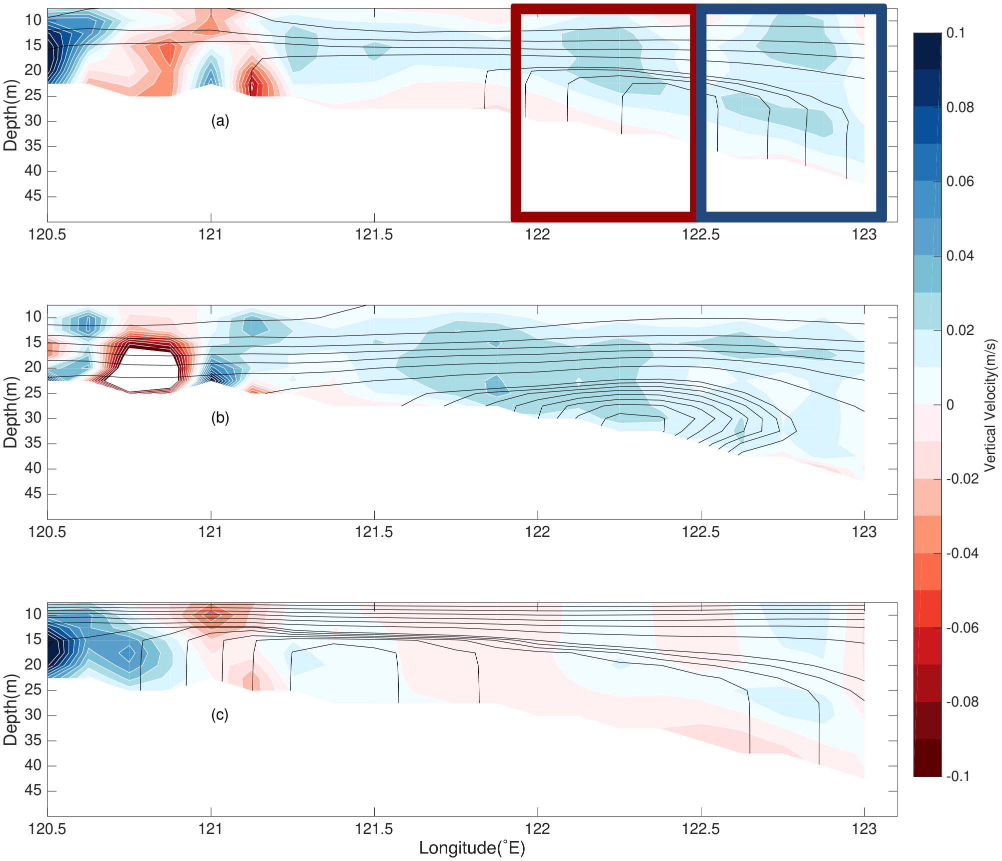

Figure 15. The temperature (lines) and zonal–vertical current (contours) along the 35.625°N profile in May in the ensemble means. For better visualization, the vertical velocity is multiplied by 1000 (unit: m/s). (a) Control run, (b) no-tide experiment, and (c) no-wind experiment.

These results validate our hypothesis that upwelling in the western portion (121.5-122°E) is influenced mainly by wind forcings; for the eastern portion (122.625-123°E), wind forcings still play a role, but tidal forcings contribute more to upwelling. The upwelling caused by the wind forcing can be explained by Ekman theory because of the predominant southeasterly monsoon, and the upwelling contributed by the tidal forcing is due to the tide-induced front, which affects the horizontal and vertical (Figs. 5a and 5b) temperature distributions. Lü et al. (2010) explained the tidal effect on upwelling, which indicates that the tide-induced front in the control run generates a relatively large baroclinic pressure gradient, which further triggers distinct upwelling. In this work, we found that such an explanation can also explain the upwelling around the Qingdao cold water mass.

Previous research has also studied upwelling and vertical secondary circulation in the Bohai and Yellow Seas and revealed that upwelling usually occurs in shallow areas along coasts, such as the Subei area and the region near the Korean Peninsula

(Lü et al., 2010; Wei et al., 2019). However, a refined analysis of the Qingdao cold water mass is still needed. Hence, in this study, we analyzed the upwelling structure in this area and explored the effects of wind and tidal forcings on upwelling.

5. Conclusions

On the basis of numerical models, the main characteristics and related dynamic processes of the local seasonal anticyclonic circulation around the Qingdao cold water mass during spring and summer were analyzed in this paper. The Qingdao cold water mass emerges in April and is fully developed in May, combined with a seasonal anticyclonic circulation. Two major scientific questions mentioned in the introduction are answered: (1) The Qingdao cold water mass is not the direct reason for the seasonal anticyclonic circulation around the Qingdao cold water mass. (2) Both tidal forcing and wind forcing play roles in horizontal anticyclonic circulation. When wind forcing is not considered, the current's general magnitude weakens, particularly on the western side of the seasonal anticyclonic circulation (northward current), confirming again that the southeasterly wind along the Shandong Peninsula is the cause of the northward current on the west side of the Qingdao cold water mass. Additionally, when tidal forcing is not considered, the eastern side of the seasonal anticyclonic circulation direction reverses, changing from a southward current to a northward current. Vertically, the tidal front causes a baroclinic pressure gradient force, which further triggers upwelling; wind forcing contributes to Ekman upwelling in the western portion (121.5-122°E).

In this paper, we use the model result of 2019 as an example. Huang et al. reported similar basic characteristics of the temperature and salinity of the Qingdao cold water mass in 2010 (2019). Currently, we limit ourselves to the simulation of 2019; in the future, we plan to discuss the interannual variation characteristics and mechanisms of the interannual variation in this anticyclonic circulation.

In addition to the insight gained regarding the dynamics of the Qingdao water mass, another innovative aspect of this paper is the demonstration of how to separate between random variations and signals in marginal seas caused by the experimental set-up. The method itself was introduced in the climate sciences in 1974 (Chervin et al., 1974), but it is rarely used when evaluating the results of numerical experiments in marginal seas.

Author contributions. LL formulated all the simulations, analyzed the results, and wrote the manuscript. HvS provided guidance and wrote and revised the manuscript, particularly the statistical test portion. DY helped with the numerical model momentum balance output and provided guidance in drafting and revising the manuscript.

***Competing interests*.** The contact author has declared that none of the authors has any competing interests.

Acknowledgments. We are grateful to the German Climate Center (DKRZ) for providing computer resources. Yang Ding was supported by the National Natural Science Foundation (NSFC, No. 42130403 and 42076010).

Data availability. The datasets generated during and/or analyzed during the current study are available from the corresponding author upon reasonable request.

References

Chen, C., Liu, H., and Beardsley, R. C.: An Unstructured Grid, Finite-Volume, Three-Dimensional, Primitive Equations Ocean Model: Application to Coastal Ocean and Estuaries, J. Atmos. Oceanic Technol., 20, 159–186, https://doi.org/10.1175/1520-0426(2003)020<0159:AUGFVT>2.0.CO;2, 2003.

Chen, C., Beardsley, R., and Cowles, G.: An Unstructured Grid, Finite-Volume Coastal Ocean Model (FVCOM) System, Oceanog., 19, 78–89, https://doi.org/10.5670/oceanog.2006.92, 2006.

Chervin, R. M., Gates, W. L., and Schneider, S. H.: The Effect of Time Averaging on the Noise Level of Climatological Statistics Generated by Atmospheric General Circulation Models, J. Atmos. Sci., 31, 2216–2219, https://doi.org/10.1175/1520-0469(1974)031<2216:TEOTAO>2.0.CO;2, 1974.

Choi, B. H.: A Tidal Model of the Yellow Sea and the Eastern China Sea, Korea Ocean Research and Development Institute, 1980.

Choi, B. H., Eum, H. M., and Woo, S. B.: A synchronously coupled tide–wave–surge model of the Yellow Sea, Coastal Engineering, 47, 381–398, https://doi.org/10.1016/S0378-3839(02)00143-6, 2003.

Diao, X.: The study of Yellow Sea Warm Current, Yellow Sea Cold Water Mass and their evolution process in sping, Institute of Oceanology, Chinese Academy of Sciences, Qingdao, 2015.

Egbert, G. D. and Erofeeva, S. Y.: Efficient Inverse Modeling of Barotropic Ocean Tides, J. Atmos. Oceanic Technol., 19, 183–204, https://doi.org/10.1175/1520-0426(2002)019<0183:EIMOBO>2.0.CO;2, 2002.

Ho, C., Wang, Y., Lei, Z., and Xu, S.: A prelimenary study of the formation of Yellow Sea Cold Mass and its properties., Oceanologia Et Limnologia Sinica, 2, 11—15, 1959.

Huang, H., Chen, X., and Lin, L.: Evolution and mechnism of the Qingdao Cold Water Mass, Oceanologia Et Limnologia Sinica, 50, 1191–1200, 2019.

Hur, H. B., Jacobs, G. A., and Teague, W. J.: Monthly variations of water masses in the Yellow and East China Seas, Journal of Oceanography, 56, 359, 2000.

Lin, L., von Storch, H., Guo, D., Tang, S., Zheng, P., and Chen, X.: The effect of tides on internal variability in the Bohai and Yellow Sea, Dynamics of Atmospheres and Oceans, 98, 101301, https://doi.org/10.1016/j.dynatmoce.2022.101301, 2022.

Lin, L., Von Storch, H., Chen, X., Jiang, W., and Tang, S.: Link between the internal variability and the baroclinic instability in the Bohai and Yellow Sea, Ocean Dynamics, 73, 793–806, https://doi.org/10.1007/s10236-023-01583-7, 2023.

Liu, G. M., Wang, H., Sun, S., and Han, B. P.: Numerical study on density residual currents of the Bohai Sea in summer, Chin. J. Oceanol. Limnol., 21, 106–113, 2003.

Lü, X., Qiao, F., Xia, C., Wang, G., and Yuan, Y.: Upwelling and surface cold patches in the Yellow Sea in summer: Effects of tidal mixing on the vertical circulation, Continental Shelf Research, 30, 620–632, https://doi.org/10.1016/j.csr.2009.09.002, 2010.

Mellor, G. L. and Yamada, T.: Development of a turbulence closure model for geophysical fluid problems, Rev. Geophys., 20, 851, https://doi.org/10.1029/RG020i004p00851, 1982.

Moon, J.-H., Hirose, N., and Yoon, J.-H.: Comparison of wind and tidal contributions to seasonal circulation of the Yellow Sea, J. Geophys. Res., 114, C08016, https://doi.org/10.1029/2009JC005314, 2009.

Penduff, T., Llovel, W., Close, S., Garcia-Gomez, I., and Leroux, S.: Trends of Coastal Sea Level Between 1993 and 2015: Imprints of Atmospheric Forcing and Oceanic Chaos, Surv Geophys, 40, 1543–1562, https://doi.org/10.1007/s10712-019-09571-7, 2019.

Saha, S., Moorthi, S., Wu, X., Wang, J., Nadiga, S., Tripp, P., Behringer, D., Hou, Y.-T., Chuang, H., Iredell, M., Ek, M., Meng, J., Yang, R., Mendez, M. P., Van Den Dool, H., Zhang, Q., Wang, W., Chen, M., and Becker, E.: The NCEP Climate Forecast System Version 2, Journal of Climate, 27, 2185–2208, https://doi.org/10.1175/JCLI-D-12-00823.1, 2014.

Wan, X. G., Bao, X., Wu, D., and Jiang, H.: Numerical diagnostic simulation of summertime tide-induced, wind-driven and thermohaline currents in the Bohai Sea, Oceanologia Et Limnologia Sinica, 35, 47–53, 2004.

Wang, B., Hirose, N., Kang, B., and Takayama, K.: Seasonal migration of the Yellow Sea Bottom Cold Water, J. Geophys. Res. Oceans, 119, 4430–4443, https://doi.org/10.1002/2014JC009873, 2014.

Wei, H., Shi, J., Lu, Y., and Peng, Y.: Interannual and long-term hydrographic changes in the Yellow Sea during 1977–1998, Deep Sea Research Part II: Topical Studies in Oceanography, 57, 1025–1034, https://doi.org/10.1016/j.dsr2.2010.02.004, 2010.

Wei, Q., Wang, B., Yao, Q., Yu, Z., Fu, M., Sun, J., Xu, B., Xie, L., and Xin, M.: Physical-biogeochemical interactions and potential effects on phytoplankton and Ulva prolifera in the coastal waters off Qingdao (Yellow Sea, China), Acta Oceanol. Sin., 38, 11–23, https://doi.org/10.1007/s13131-019-1344-3, 2019.

Xia, C., Qiao, F., Yang, Y., Ma, J., and Yuan, Y.: Three-dimensional structure of the summertime circulation in the Yellow Sea from a wave-tide-circulation coupled model, J. Geophys. Res., 111, C11S03, https://doi.org/10.1029/2005JC003218, 2006.

Xia, J. and Xiong, X.: Distributions and seasonal changes of water temperature in the Bohai Sea, Yellow Sea and East China Sea., Advances in Marine Science, 31, 55–68, 2013.

Xu, D. and Zhao, B.: Existential proof and numerical study of a mesoscale anticyclonis eddy in the Qingdao-Shidao offshore, Acta Oceanologica Sinica, 18–26, 1999.

Yu, F., Zhixin, Z., Diao, X., Guo, J., and Ge, R.: Analysis of water temperature distribution characteristics in the Southern Yellow Sea in spring, Advances in Marine Science, 23, 281–288, 2005.

Yu, F., Zhang, Z., Diao, X., Guo, J., and Tang, Y.: Analysis of evolution of the Huanghai Sea Cold Water Mass and its relationship with adjacent water masses, Acta Oceanologica Sinica, 05, 26–34, https://doi.org/CNKI:SUN:SEAC.0.2006-05-002., 2006.

Yuan, D., Li, Y., Qiao, F., and Zhao, W.: Temperature inversion in the Huanghai Sea bottom cold water in summer, Acta Oceanol. Sin., 32, 42–47, https://doi.org/10.1007/s13131-013-0287-3, 2013.

Zhang, cunyi: Analysis of the strength and yearly vairations of Qingdao cold water-masses, Marine Sciences, 10, 48–51, 1986.

Zhang, F., Mao, H., and Leng, Y.: Analysis of drift bottle and drift card experiments in Bohai Sea and Huanghai Sea (1975–80), Chin. J. Ocean. Limnol., 5, 67–72, https://doi.org/10.1007/BF02848524, 1987.

Zhang, Q., Yang, Y., and Cheng, M.: An analysis of characteristics of thermohaline structures in the South Yellow Sea in spring, Haiyang Xuebao, 18, 50–55, 1994.

Zhang, Q., Liu, X., Cheng, M., and Y, X.: Characteristics and formation causes of Qingdao cold water mass, Chinese Journal of Oceanology and Limnology, 20, 303–308, 2002.

Zhang, Q., Hou, Y., Cheng, M., Liu, X., and Yin, B.: Variation Features in Qingdao Cold Water Mass Strength, Studia Marina Sinica, 46, 13–21, 2004.

Zhang, Y. and Geng, X.: Relationship between fishery and hydrological situation, Hydrological regime in Shandong coastal waters. Ji-nan:Shandong Map Press, 71–87 pp., 1989.

Zheng, D. and Zhang, R.: Analysis of spring water masses in the sea area off Yantai, Weihai, and Shidao., Marine Science Bulletin, 01, 61–68, 1983.

Zhou, F., Huang, D., Xue, H., Xuan, J., Yan, T., Ni, X., Zeng, D., and Li, J.: Circulations associated with cold pools in the Bohai Sea on the Chinese continental shelf, Continental Shelf Research, 137, 25–38, https://doi.org/10.1016/j.csr.2017.02.005, 2017.

Zhu, P. and Wu, H.: Origins and transports of the low-salinity coastal water in the southwestern Yellow Sea, Acta Oceanol. Sin., 37, 1–11, https://doi.org/10.1007/s13131-018-1200-x, 2018.

Zhang, Q., and Liu, Z, Qi, J., Zhou D., and Zheng D. : Study on the extinction mechanism for Qingdao cold water mass, Haiyang Xuebao, 38, 27–33, 2016.

Appendix

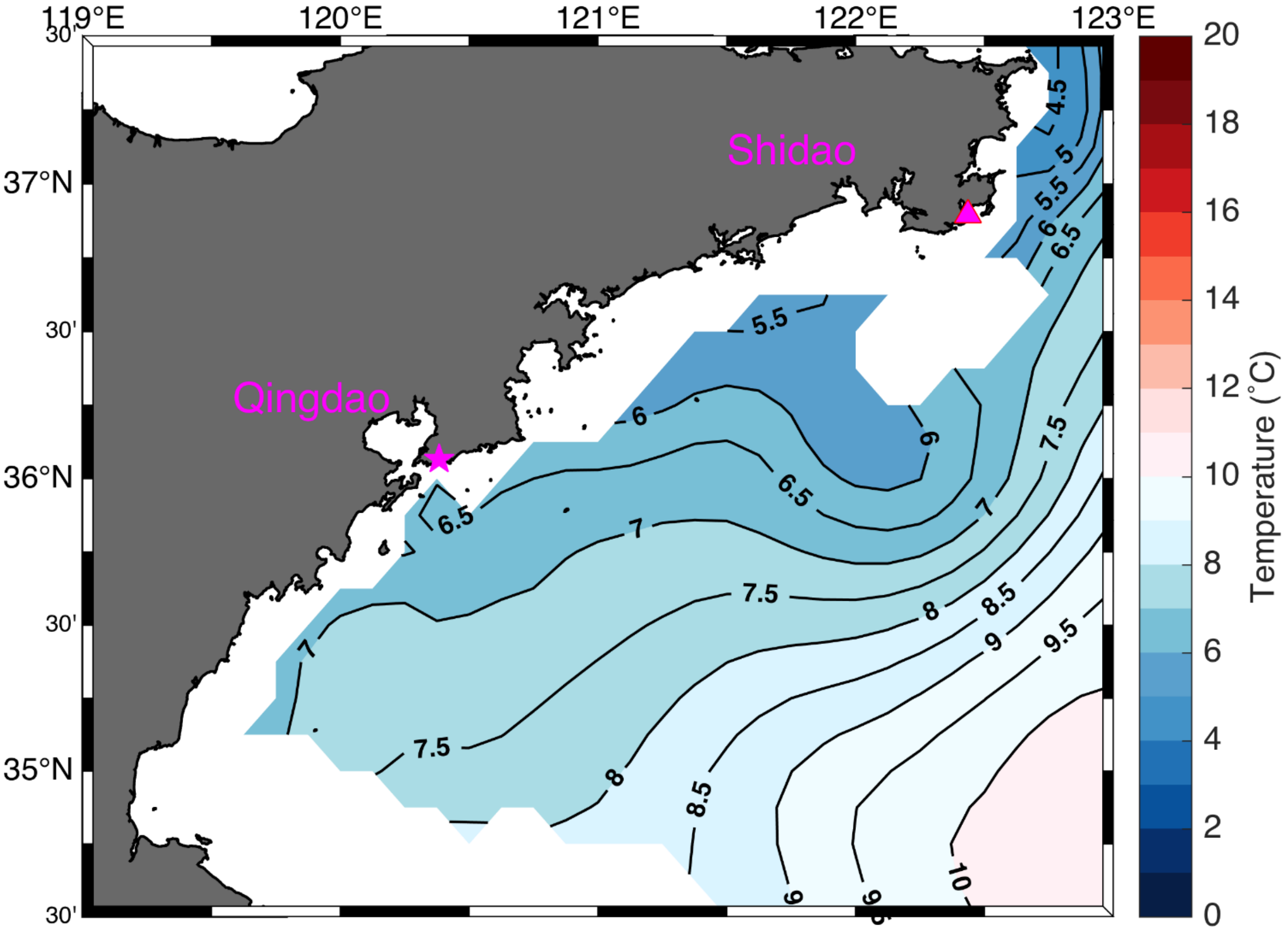

Figure A1. The monthly mean temperature evolution of the Qingdao cold water mass in March at a depth of 25 m, as derived from the ensemble mean of the control runs.

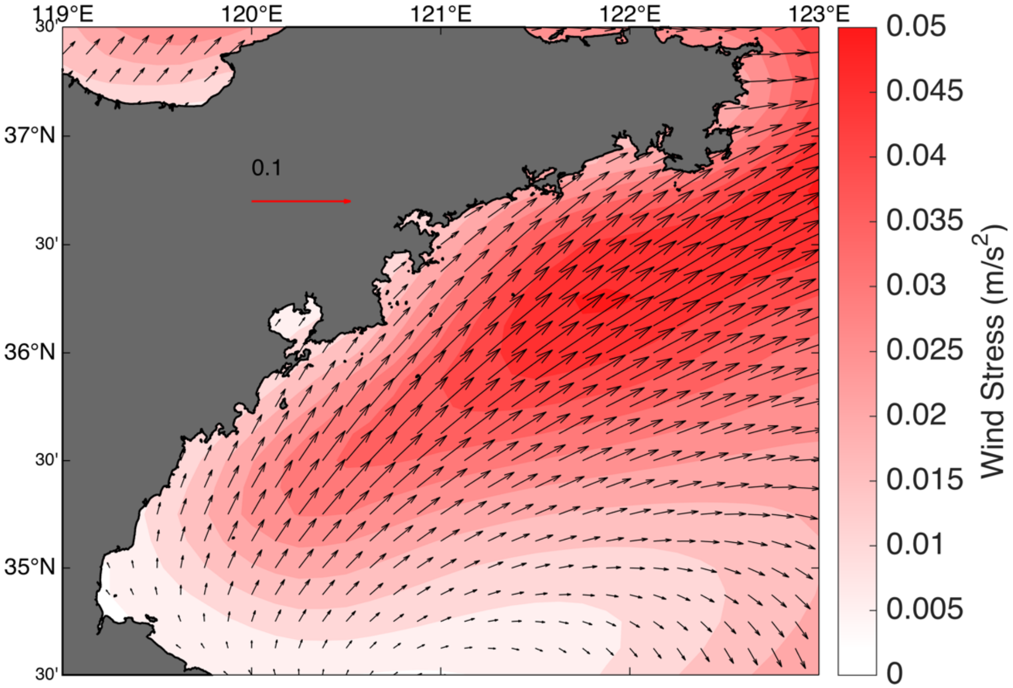

Figure A2. Mean surface wind stress of May 2019 used in the control run and the no-tide ensembles.

495